IVYSPRING INTERNATIONAL PUBLISHER

Theranostics

2018; 8(6): 1665-1677. doi: 10.7150/thno.22469

Research Paper

Porphyrin-grafted Lipid Microbubbles for the Enhanced Efficacy of Photodynamic Therapy in Prostate Cancer through Ultrasound-controlled *In Situ* Accumulation

Yujia You[1,*], Xiaolong Liang[2,*], Tinghui Yin[1], Min Chen[3], Chen Qiu[1], Chuang Gao[3], Xiaoyou Wang[3], Yongjiang Mao[1], Enze Qu[1], Zhifei Dai[3]✉ and Rongqin Zheng[1]✉

1. Department of Medical Ultrasonic, The Third Affiliated Hospital of Sun Yat-sen University, Guangzhou 510630, China
2. Department of Ultrasound, Peking University Third Hospital, Beijing 100191, China
3. Department of Biomedical Engineering, College of Engineering, Peking University, Beijing 100871, China

*These authors contributed equally to this work.

✉ Corresponding authors: Z.D. (email: zhifei.dai@pku.edu.cn) or to R.Z. (email: zhengrq@mail.sysu.edu.cn)

© Ivyspring International Publisher. This is an open access article distributed under the terms of the Creative Commons Attribution (CC BY-NC) license (https://creativecommons.org/licenses/by-nc/4.0/). See http://ivyspring.com/terms for full terms and conditions.

Received: 2017.08.21; Accepted: 2017.12.23; Published: 2018.02.12

Abstract

Photodynamic therapy (PDT) holds promise for focal therapy of prostate cancer (PCa). However, the therapeutic efficacy needs improvement, and further development of PDT for PCa has challenges, including uncertainty of photosensitizers (PSs) accumulation at the tumor site and difficulty in visualizing lesions using conventional ultrasound (US) imaging. We have developed novel porphyrin-grafted lipid (PGL) microbubbles (MBs; PGL-MBs) and propose a strategy to integrate PGL-MBs with US imaging to address these limitations and enhance PDT efficacy.

Methods: PGL-MBs have two functions: imaging guidance by contrast-enhanced ultrasound (CEUS) and targeted delivery of PSs by ultrasound targeted microbubble destruction (UTMD). PGL-MBs were prepared and characterized before and after low-frequency US (LFUS) exposure. Then, *in vitro* studies validated the efficacy of PDT with PGL-MBs in human prostate cancer PC3 cells. PC3-xenografted nude mice were used to validate CEUS imaging, accumulation at the tumor site, and *in vivo* PDT efficacy.

Results: PGL-MBs showed good contrast enhancement for US imaging and were converted into nanoparticles upon LFUS exposure. The resulting uniquely structured nanoparticles avoided porphyrin fluorescence quenching and efficiently accumulated at the tumor site through the sonoporation effect created with the assistance of US to achieve excellent PDT efficacy.

Conclusions: This is the first preclinical investigation of MBs applied in PDT for PCa. PGL-MBs possess favorable CEUS imaging effects to enhance the localization of tumors. PGL-MBs with LFUS control PS accumulation at the tumor site to achieve highly effective PDT of PCa. This strategy carries enormous clinical potential for PCa management.

Key words: porphyrin-grafted lipid, microbubbles, photosensitizer, ultrasound-targeted microbubble destruction, photodynamic therapy

Introduction

Prostate cancer (PCa) is one of the most common malignancies and a leading cause of cancer-related deaths in many western countries, such as the USA [1]. In China, PCa has also become the fastest growing cancer in recent years [2]. Conventional radical treatment (surgery or radiotherapy) for PCa patients could generate lifestyle-altering complications, such as sexual, urinary, and gastrointestinal side effects, that seriously alter the quality of life in approximately 15–20% of patients [3]. However, almost half of newly

diagnosed PCa patients are low-risk [4], and radical therapies are thought to be aggressive for these lesions, triggering widespread protests against over-treatment in PCa management [5]. Photodynamic therapy (PDT) has been used in the treatment of PCa as a promising focal therapy, which could maintain the delicate balance between the risks and benefits of treatment.

PDT uses light to activate photosensitizers (PSs) to transfer energy to tissue oxygen, generating reactive oxygen species that are directly responsible for tissue destruction [6]. Since its first application in skin tumor therapy in 1903 [7], PDT has become a potential alternative treatment for many tumors due to its well-recognized selectivity, safety and repeat-ability [8]. With the increasing number of clinical trials for PCa treatment [9-11], PDT has been attracting increasing attention. A phase III clinical trial demonstrated that PDT results in less disease progression than active surveillance and has few serious complications, and thus PDT may be a safe and effective treatment for low-risk, localized PCa [12]. However, there are still limitations to current PDT methods for PCa, which should be addressed to further improve PDT efficacy, thus enhancing the confidence of patients with low- to moderate-risk localized prostate cancer to undergo focal therapy.

One limitation is the uncertainty of PS accumulation at the tumor site. PSs are key in the PDT process, and accumulation of PSs at the tumor site is an important precondition for achieving selective treatment and reducing side effects. Clinically used PSs are often administered intravenously and laser irradiation is conducted when the PS concentration reaches the maximum value at the tumor site. However, *in vivo* PS distribution is still uncontrollable, which results in uncertain therapeutic effects, and thus, selectively delivering PSs to tumors remains a great challenge [13].

Another limitation is the difficulty in visualizing PCa lesions using conventional ultrasound (US) imaging. Imaging guidance plays an imperative role because it could provide not only accurate identification of lesions but also accurate monitoring of the identified target volume to assess the therapeutic effects, thus helping to reduce the risk of complications and improve the therapeutic efficiency [14]. However, displaying the lesions is difficult when using conventional US (2D-US or color doppler) to guide PDT. Thus, improving conventional US imaging is necessary [15].

Microbubbles (MBs) are widely used in clinical diagnosis. As contrast agents for US imaging, MBs could enhance the sensitivity of lesion visualization and diagnosis specificity in various tumors [16-18]. Furthermore, MBs are excellent platforms for cancer treatment. By virtue of their responsiveness (namely, cavitation effect) to US irradiation, which is so-called ultrasound targeted microbubble destruction (UTMD) [19, 20], MBs could achieve targeted delivery of various drugs. Thus, MBs are actually a good candidate for assisting PDT in PCa, for their enhanced contrast, which can help to better localize lesions, and targeted delivery of PSs, which is the crux of improving PDT selectivity.

However, few studies have focused on PSs (mainly porphyrin or its derivatives [21]) combined with MBs for PDT. We speculate there are two possible reasons: (1) insufficient drug loading content of MBs, and (2) poor accumulation at tumor sites. Due to the structure of the MB, which consists of a gas core and monolayer lipid, loading hydrophilic drugs is challenging, and it has a very limited loading space for hydrophobic drugs [22]. In addition, due to their large size, MBs are often confined in blood vessels, and it is difficult for MBs to pass through the gap between epithelial cells of tumor vessels, resulting in poor accumulation at the tumor site.

The porphyrin-grafted lipid (PGL), consisting of double carbon chains and porphyrin, can self-assemble into nanoparticles and shows high drug loading content of above 33% and strong fluorescence due to its superior structure [23-25]. To overcome the dilemma of MBs used in PDT, PGL was herein used to fabricate MBs (PGL-MBs) by mixing with inert fluorocarbon gas, resulting in a stable monolayer-covered MB with high porphyrin loading efficiency. Such functional MBs can be detected in real-time by US imaging. In addition, select accumulation of PS in the tumor tissue can be easily accomplished by applying the UTMD technique, which could efficiently covert PGL-MBs into PGL-loaded nanoparticles (PGL-NPs) and help PSs accumulate in the tumor tissue through the sonoporation effect. Therefore, these novel PGL-MBs could achieve effective PDT (Figure 1) and show great potential for cancer theranostics.

Methods

Chemicals and reagents

The following powdered phospholipids (Avanti Polar Lipids Inc., USA) were used in this study without further purification: 1,2-distearoyl-sn-glycero-3-phosphoethanolamine-N-[methoxy(polyethylene glycol)-2000] [DSPE-PEG; molecular weight (MW): 2805.5] and 1,2-distearoyl-sn-glycero-3-phosphocholine (DSPC; MW: 790.2). Organic reagents such as chloroform were obtained from Beijing Chemical (Beijing, China). Deionized (DI) water was

obtained using a Milli-Q Water Purification system. 6-carboxy-2′,7′-dichlorodihydrofluorescein diacetate (Carboxy-H_2DCFDA) was purchased from Invitrogen (USA). Cell counter kit-8 (CCK-8) was supplied by KeyGEN (Nanjing, China). Human prostate cancer PC-3 cells and human umbilical vein endothelial cells (HUVECs) were purchased from the Cell Bank of Shanghai Institutes for Biological Sciences, Chinese Academy of Sciences (Shanghai, China). All the BALB/c nude mice were purchased from Vital River Laboratories Animal Technology (Beijing, China).

Preparation of PGL-MBs

PGL-MBs were prepared using a thin-film hydration-sonication method. Briefly, a mixture containing 15 mol% PGL, 50 mol% DSPC, 30 mol% cholesterol and 5 mol% DSPE-PEG2000 was dissolved in 2-5 mL of chloroform ($CHCl_3$), which was then removed by a rotary evaporator to form a thin film on the wall of the vial, and dried in a vacuum overnight. Then, the dried film was re-hydrated with 1 mL of phosphate buffered saline (PBS), followed by incubation in a water bath at 60°C for 30 min, vortexing for 20 min and then sonication for 3 min with a probe-type sonicator until a clear and transparent solution was obtained. The liposomal suspension was then transferred into a small sample vial, and the air above the solution was replaced with perfluoropropane (C_3F_8) gas. Next, the solution was mechanically agitated for 45 s using a VialMix shaker. To purify the PGL-MBs, they were gently shaken and transferred into a centrifuge tube, followed by separating from residual nanoparticles by centrifugation at 129 × g for 5 min. Then the MBs was washed with ultrapure water and finally dispersed in PBS buffer.

Characterization of PGL-MBs

UTMD was carried out using LFUS (1 MHz, pulse repetition frequency 1 kHz with a 50% duty cycle, acoustic pressure 400 kPa), which was generated by a therapeutic US system (DCT-700, WELLD, Shenzhen, China). Fluorescent images of PGL-MBs were acquired using a fluorescence microscope (Leica DMI3000B). The size distribution and concentration of PGL-MBs were measured using a Coulter counter (Multisizer 3 Coulter Counter, Beckman Coulter, Inc., USA). Dynamic light scattering (DLS) measurements were performed using a 90Plus/BI-MAS instrument (Brookhaven Instruments Co., USA). The sample for transmission electron microscopy (TEM) was prepared by immersing a formvar-coated copper grid into the PGL-NPs suspension (0.5 mg/mL). After 10 min of incubation, samples were blotted away and the grids were negatively stained with freshly prepared and sterile-filtered 2% (w/v) phosphotungstic acid aqueous solution for 10 min at room temperature. The grid was then washed with distilled water and dried in air. Finally, TEM images were obtained using a FEI TECNAI G2 20 high-resolution transmission electron microscope operating at 200 kV. Ultraviolet-Visible (UV-Vis) spectra and fluorescence spectra were obtained using a UV-Vis spectrophotometer (Evolution 220, Thermo Scientific) and a Varian Cary Eclipse fluorescence spectrophotometer (Lumina, Thermo Scientific), respectively.

CEUS and fluorescence imaging

In vitro CEUS experiments were carried out using a custom-made 2% (w/v) agarose mold as designed in a previous study [26]. Different concentrations of PGL-MBs (1×10^7/mL, 5×10^6/mL, 2×10^6/mL, and 1×10^6/mL) were used for harmonic imaging using a clinical US system (DC8, Mindray Medical International Co., Ltd. China). Then, the samples were exposed to LFUS for 2-3 min (1 MHz, pulse repetition frequency 1 kHz with a 50% duty cycle, acoustic pressure 400 kPa), which was generated by a therapeutic US system (DCT-700, WELLD, Shenzhen, China). *In vivo* CEUS were performed using the same machine as the *in vitro* experiments and 10 μL PGL-MBs (1 mg/mL) were injected intravenously. To determine the *in vivo* circulation half-life of PGL-MBs, the abdominal aorta was circled as the region of interest (ROI). CEUS videos, starting when PGL-MBs were injected and continuing at least for 10 min, were recorded for the offline generation of time-intensity curves and quantitative analyses by using the CEUS quantitative analyzing software Sonamath (AmbitionT.C., China). For fluorescence imaging *in vivo*, mice were imaged using an IVIS Spectrum In Vivo Imaging System (Caliper Life Sciences).

Detection of singlet oxygen ($^1O_2$) *in vitro*.

Generation of $^1O_2$ was detected chemically using the disodium salt of 9,10-anthracenedipropionic acid (ADPA, Sigma) as an $^1O_2$ sensor. ADPA is bleached by $^1O_2$ to its corresponding endoperoxide. The reaction was monitored spectrophotometrically by recording the absorbance decline of ADPA solution at 378 nm. ADPA in H_2O was mixed with PGL-MBs and PGL-NPs in H_2O, separately. Free porphyrin (1% DMSO/H_2O) and PBS were used as the control samples. The absorbance of the original ADPA solution was adjusted to approximately 2.25 at 378 nm, and the absorbances of free porphyrin, PGL-MBs and PGL-NPs were adjusted to 0.65 at 420 nm. The

solutions were irradiated with a 650±5 nm laser source, and their optical densities at 378 nm were recorded every 5 min using a UV-Vis spectrophotometer.

For cell assays of $^1O_2$ detection, there were 8 groups: (1) PGL-MBs+LFUS+laser; (2) PGL-MBs+LFUS; (3) PGL-MBs+Laser; (4) PGL-MBs only; (5) PBS+LFUS+laser; (6) PBS+LFUS; (7) PBS+Laser; (4) PBS only. The PC-3 cells were routinely cultured in RPMI-1640 medium (Roswell Park Memorial Institute-1604; GIBCO) with 10% fetal bovine serum (FBS) and seeded on 96-well plates at a density of 5×10^3 cells/well. After the cells were incubated for 24 h, the medium was replaced with 80 μL fresh culture medium. Then, 20 μL solution (PGL-MBs or PBS) was added to the well with or without LFUS exposure for 2 min. The cells were further incubated for 4 h at 37°C and 5% CO_2. The final concentration of PGL was 5 μM. After washing once with PBS, the cells were incubated with 100 μL carboxy-H_2DCFDA (25 mM) for 10 min. Subsequently, the cells were washed once with PBS and irradiated by a 650±5 nm laser (200 mW/cm^2) for 2 min per well. Then, the fluorescence emission of 5(6)-carboxy-2′,7′-dichlorofluorescein (carboxy-DCF; Excitation/Emission=495/529 nm) was immediately measured using a fluorescence microscope (Leica DMI3000B).

In vitro PDT efficacy assay

For quantitative evaluation, the PC-3 cells were seeded on 96-well plates at a density of 5×10^3 cells/well and grown overnight. There were 4 treatments: (1) PGL-MBs+LFUS+laser; (2) PGL-MBs+LFUS; (3) PGL-MBs+laser; (4) PGL-MBs only. Different concentrations of PGL-MBs (ranging from 0 to 2 mM PGL, as evaluated by UV-Vis absorption measurements) were added to the designated wells, and LFUS irradiation was performed or not, according to the group. After incubation for 4 h in the dark at 37°C, the wells were carefully rinsed three times with sterile PBS, and 0.2 mL of fresh medium was added to each well. Then, the wells were immediately irradiated for 10 min with broadband visible light using a xenon lamp (150 W) equipped with a filter passing light of 400-700 nm (The power at the cell level was 180 J/cm^2) (25). Finally, the plates were incubated at 37°C in the dark overnight. Cell viability was estimated using a CCK-8 assay. The spectrophotometric absorbance was measured with a microplate reader (Synergy HT, BioTek), and the analysis was performed in triplicate.

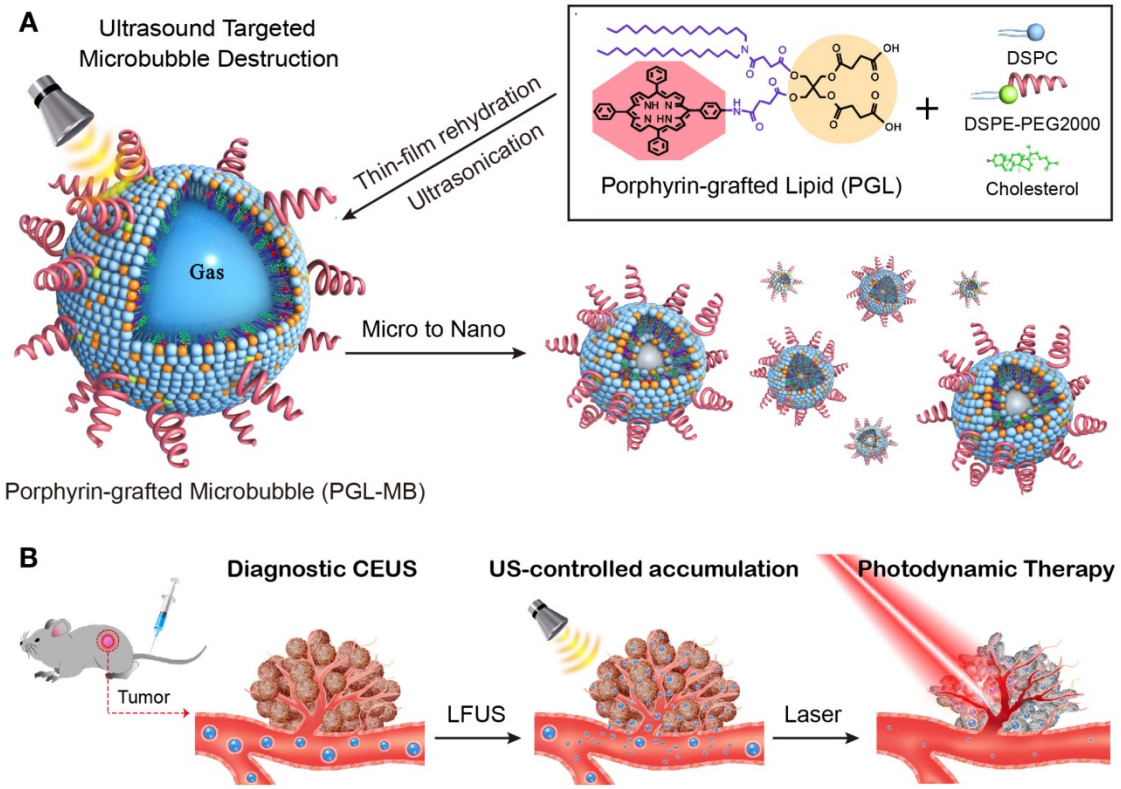

Figure 1. Schematic of the microbubble-based, ultrasound-assisted PDT strategy. (A) Preparation of PGL-MB and its transformation from microbubbles to nanoparticles under exposure to low-frequency ultrasound (LFUS). (B) Experimental process of *in vivo* PDT under the guidance of contrast enhance ultrasound (CEUS) imaging, followed by ultrasound targeted microbubble destruction (UTMD).

For qualitative evaluation, the PC-3 cells were seeded on 12-well plates at a density of 5×10^4 cells/well and given 4 different treatments separately: (1) PGL-MBs+LFUS; (2) PGL-MBs; (3) PBS+LFUS; (4) PGL-MBs only. 650±5 nm laser (200 mW/cm^2) was used to irradiate the center of every well for 10 min and the surrounding area of the well was shielded from light. Then calcein acetoxymethyl ester (calcein-AM) and propidium iodide (PI) co-staining was performed for 10 min and the fluorescence was immediately measured using a fluorescence microscope.

In vivo therapeutic efficacy of PDT in PC-3 tumor-bearing nude mice

Male BALB/c athymic nude mice (5-6 weeks old) were used under protocols approved by the Institutional Animal Care and Use Committee of Peking University. To develop subcutaneous PC-3 tumors, 1×10^7 PC-3 cells suspended in 100 μL FBS-free RPMI-1640 medium were subcutaneously injected into the back of each mouse. Mice were divided into eight groups for the treatments (n=9 each): (1) PGL-MBs only; (2) PGL-MBs+LFUS; (3) PGL-MBs+ laser; (4) PGL-MBs+LFUS+laser; (5) PBS only; (6) PBS+LFUS; (7) PBS+laser; (8) PBS+LFUS+laser. 100 μL PGL-MBs and PBS was injected intravenously. For the mice treated by LFUS, the tumors were covered with ultrasonic coupling agent and then LFUS (DCT-700 therapeutic US system with the same parameters as those in the *in vitro* study) was applied by a probe contacting the tumor tissue through couplant. For the mice treated by laser, the optical fiber of a 650 nm laser source was placed in a holder and aligned about 1 cm away from the tumor. The laser spot size was adjusted according to the size of the tumor to ensure that the whole tumor could be irradiated by the laser.

Treatments began when the tumor volume reached 100-120 mm^3, which was designated day 0. The tumors were measured for the maximum width (X) and length (Y), and the tumor volumes (V) were calculated using the formula: $V = (X^2Y)/2$. Tumor size was measured every day using a Vernier caliper for 7 days after the first PDT treatment.

Three mice from each group were sacrificed at 24 h after treatment, and the tumors were excised and fixed with freshly prepared 10% PBS-buffered formalin for 24 h. Hematoxylin and eosin (H&E) staining of tumor tissue sections (3 mm) was performed after deparaffinization. An *in situ* terminal deoxynucleotidyl transferase-mediated nick end labeling (TUNEL) assay was carried out on the excised tumor tissues using an *in situ* cell death detection POD kit (Roche, Penzberg, Germany) in accordance with the manufacturer's instructions. In brief, tumor tissue sections were deparaffinized with xylene and ethanol and washed with TRIS-buffered saline (TBS). After 100 mL of proteinase K (20 mg/mL) in TBS was added at room temperature for 20 min, the sections were incubated with blocking solution (0.3% hydrogen peroxide (H_2O_2) in methanol) for 10 min at room temperature. Next, the slides were placed in a plastic jar containing 200 mL of 0.1 M citrate buffer (pH=6.0) with an applied 350 W microwave irradiation for 5 min. Then, the permeabilized cells on each slide were incubated with 50 mL of TUNEL reaction mixture (with terminal deoxynucleotidyl transferase, TdT enzyme) in a humidified chamber for 60 min at 37°C to catalyze the polymerization of fluorescein-labeled nucleotides to free 3′-OH (hydroxyl) DNA ends. DAPI (4′,6-diamidino-2-phenylindole) solution was used to stain the cell nuclei. Then, the slices were observed using a fluorescence microscope.

Statistical analysis.

Statistical analysis was performed by two-sided Student's t-test for two groups, and one-way analysis of variance for multiple groups. A value of $P < 0.05$ was considered statistically significant.

Results

Preparation and characterizations of PGL-MBs

PGL was synthesized according to our reported method [23]. PGL-MBs were generated from a mixture of PGL, DSPC, cholesterol and DSPE-PEG2000 at a molar ratio of 15:50:30:5 through a thin-film hydration-sonication method, followed by filling of the sample containers with perfluoro-propane and mechanical agitation for 45 s. The loaded content of porphyrin was calculated to be 18.90 wt%. Figure S1A shows that the PGL-MBs can enhance US imaging greatly and increase the US contrast signal.

To characterize the changes to PGL-MBs produced by the UTMD technique, a series of *in vitro* experiments was conducted. UTMD was carried out using LFUS. CEUS was performed to ensure the complete destruction of PGL-MBs (Figure S1A). When exposed to LFUS, the turbid PGL-MBs solution become transparent, which was also evidence of PGL-MB destruction (Figure S1B). Next, the size distribution of PGL-MBs before and after LFUS exposure was detected using a Coulter counter and by a DLS technique, respectively. The mean diameter of PGL-MBs was 0.94 μm (Figure 2A), and when exposed to LFUS, most of the resulting particles showed a diameter of less than 100 nm (Figure 2B). Furthermore, the morphology changes before and after LFUS were observed using fluorescence

microscopy and TEM, respectively (Figure 2C and 2D), validating the successful transformation of PGL-MBs into PGL nanoparticles (PGL-NPs) following LFUS, which is very important for selective PS aggregation at the tumor tissue *in vivo*.

Changes in the optical properties were also investigated using a UV-Vis spectrometer and a fluorescence spectrophotometer. As shown in Figure 2E and 2F, the absorption spectra of PGL-MBs exhibited a negligible redshift compared to free porphyrin. In addition, both the absorption and fluorescence spectra of PGL-MBs did not change after LFUS. Many conventional PSs incorporated into nanoparticles would easily aggregate and cause fluorescence self-quenching due to their π-π interactions and hydrophobic characteristics, usually resulting in a significant reduction of $^1O_2$ generation [27], which would reduce the PDT efficacy of PSs. In contrast, the position of the Soret and Q bands of porphyrin showed negligible redshift between PGL-MBs and free PGL, indicating that aggregation of porphyrin barely occurred in the PGL-MBs. Moreover, the spectra of PGL-NPs were similar to those of PGL-MBs, indicating that no further aggregation occurred during the transformation of PGL-MBs to PGL-NPs. We speculated that this phenomenon was due to insertion of the lipid carbon chain in the PGL structure, and the existence of double-alkyl chains could sterically hinder the porphyrin moieties to approach each other, preventing aggregation of the porphyrin group. This finding was very different from the reported porphyrin MBs [28], in which the orientation of the porphyrin and lysophosphatidylcholine constituents induce extensive porphyrin interactions and fluorescence quenching, thereby enhancing absorption during photoacoustic imaging. The retentive fluorescence intensity of our PGL-MBs could ensure a favorable effect for fluorescence imaging and might indicate excellent PDT efficacy.

A crucial property for photodynamic drugs is the generation of $^1O_2$, which is believed to play a paramount role in the cytotoxicity during PDT. Accordingly, the generation of $^1O_2$ was detected chemically using ADPA as a detector, which was bleached to its non-fluorescent endoperoxide form in the presence of $^1O_2$. As illustrated in Figure 3A and 3B, the absorbance of ADPA in

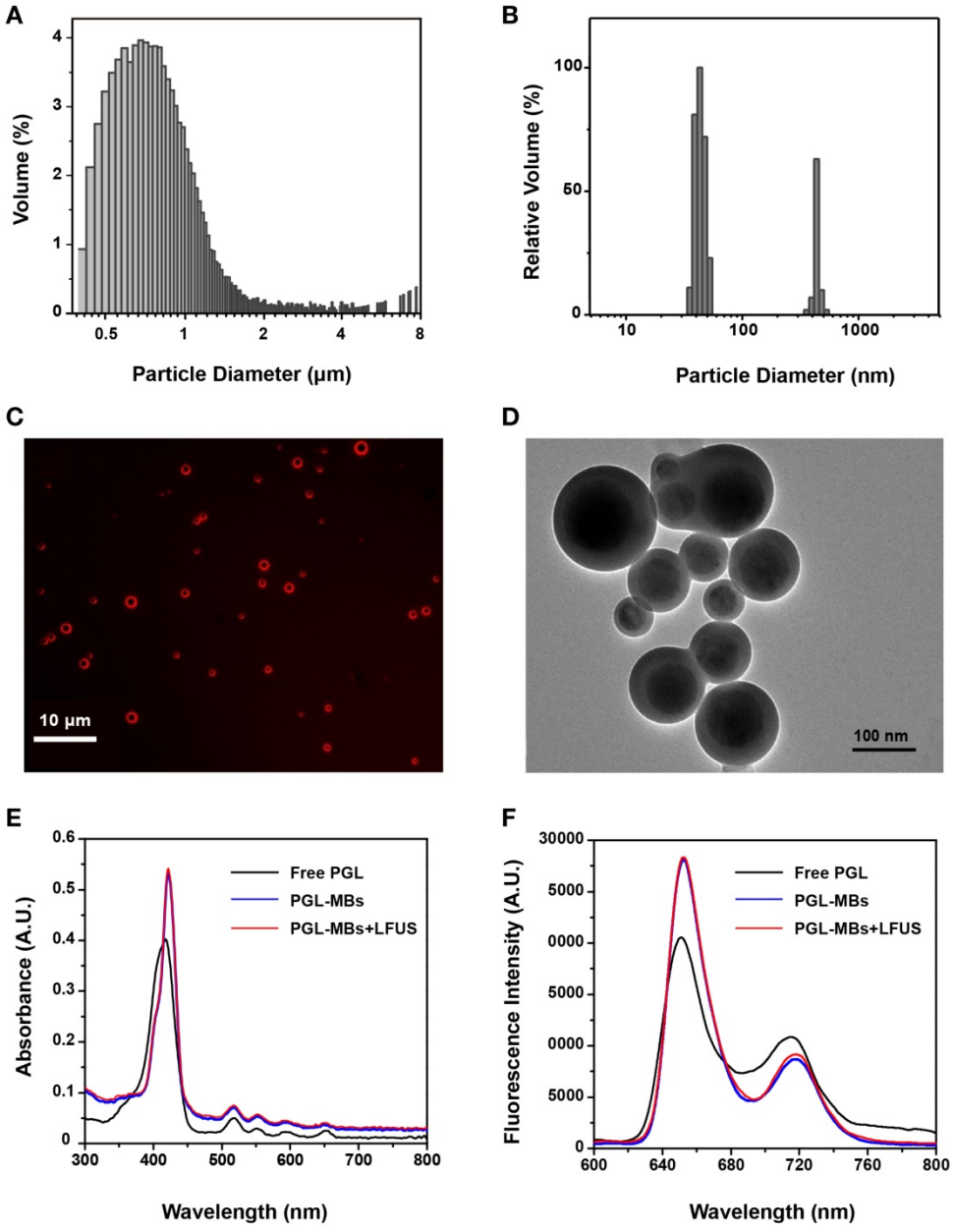

Figure 2. Characterizations of PGL-MBs before and after LFUS irradiation. Size distributions of PGL-MBs (A) and PGL-NPs (B). (C) Fluorescence images of PGL-MBs under fluorescence microscopy. (D) TEM images of LFUS-irradiated PGL-MBs. Absorption spectra (E) and fluorescence spectra (F) of PGL-MBs before and after LFUS irradiation compared with free PGL.

both PGL-MBs and PGL-NPs groups decreased rapidly as a function of light irradiation time. In stark contrast, the absorbance decreased more slowly in the presence of free PGL. Notably, the $^1O_2$ generation of PGL-NPs was slightly stronger than that of PGL-MBs. We speculated that this result may be caused by PGL-MBs floating in solution, resulting in less contact with ADPA during the detection of $^1O_2$. Moreover, for the PBS control group, ADPA absorbance produced no change under light irradiation, further confirming that the bleaching of ADPA in the presence of porphyrin was not caused by the irradiated light but by the singlet oxygen.

Cell assays

The *in vitro* PDT efficacy to cancer cells was investigated with the PC-3 tumor cell line, which was derived from human prostate cancer cells. Cellular $^1O_2$ generation was first detected using the cell-permeant ROS indicator carboxy-H_2DCFDA. After 650±5 nm laser irradiation, cells incubated with PGL-MBs displayed stronger green fluorescence, suggesting generation of more $^1O_2$ in cells incubated with PGL-MBs than in the control cells. For the control groups treated with only laser or only PGL-MBs, green fluorescence was hardly observed (Figure S2). Next, to evaluate cell viability after various treatments, calcein-AM and PI co-staining was performed to verify the PDT effect on the cancer cells. PC-3 cells were incubated with PGL-MBs with or without LFUS exposure, and laser exposure was confined to a circular area. As shown in Figure 4A, cell death could be observed (stained by PI with red fluorescence) only in the region treated with both PGL-MBs and light; PGL-MBs with LFUS exposure showed increased cell death due to enhanced uptake of PGL compared to the group without LFUS treatment. No cell death was observed with only LFUS treatment in the absence of PGL-MBs, indicating the safety of LFUS. Furthermore, the cytotoxicities of various treatments were determined using a CCK-8 assay (Figure 4B). In the case of light exposure, cell viability of PC-3 cells decreased gradually with the increasing concentrations of PGL. In addition, compared to the simple PGL-MBs+laser group, the combination treatment with LFUS (PGL-MBs+LFUS+laser group) enhanced the therapeutic effect when the concentration of PGL ranged from 0.2 μM to 1 μM ($P < 0.05$). In contrast, for the group without PGL-MBs treatment (concentration was 0 μM), no decrease in cell viability was observed in different treatments, consistent with the results of calcein-AM/PI staining.

Furthermore, the biocompatibility of the PGL-MBs was investigated using human umbilical vein endothelial cells (HUVECs) by measuring cell viability with a CCK-8 assay. HUVECs were set as two groups and incubated with different concentrations of PGL-MBs, with or without LFUS exposure. Without laser irradiation, both groups showed similarly undiminished cell viability, even when the concentration of PGL was increased to 48 μM (Figure S3). In remarkable contrast, 2 μM PGL could induce almost complete PC-3 cell death upon laser irradiation (Figure 4B). These results indicated that PGL-MBs possess excellent biocompatibility for normal human cells and that the LFUS would not induce any additional damage to normal cells.

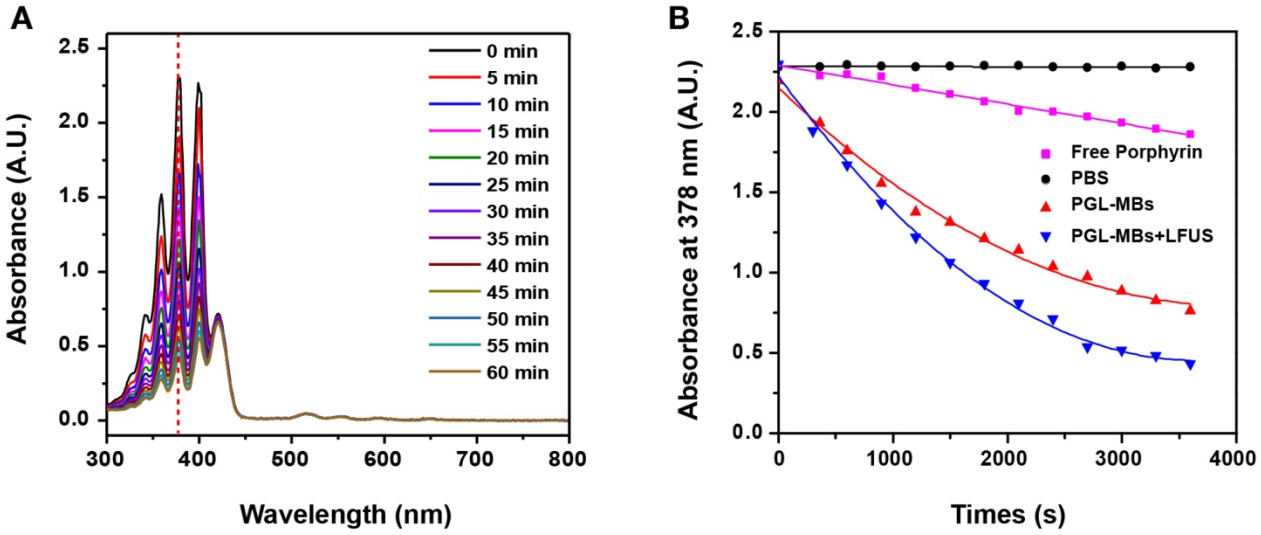

Figure 3. Detection of singlet oxygen ($^1O_2$) in solution. (A) Time-dependent bleaching of ADPA caused by $^1O_2$ generated by PGL-NPs (PGL-MBs after LFUS exposure) under laser irradiation. (B) The change in ADPA absorption at 378 nm as a function of the time of light exposure (650 nm, 200 mW/cm^2).

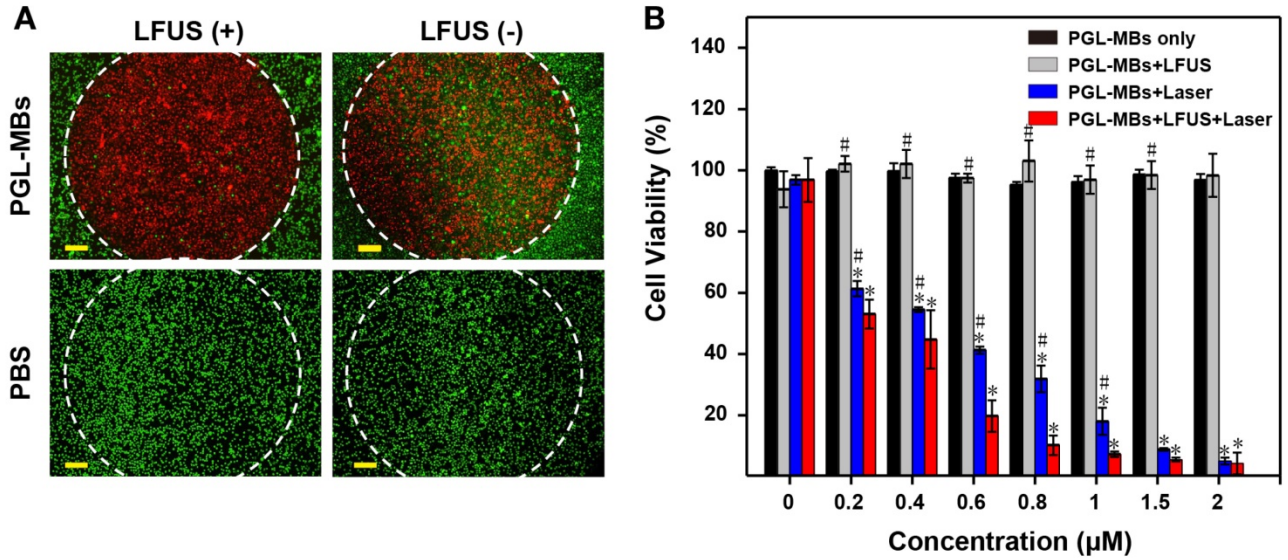

Figure 4. Evaluation of PDT efficacy by cell assays. (A) Calcein-AM/PI staining (merged images) observed by fluorescence microscopy (×10, scale bar = 100 μm). The cells were treated with PGL-MBs (containing 1 μM PGL) or PBS with or without LFUS exposure (400 kPa, 3 min). Laser irradiation (650 nm, 200 mW/cm^2) was only in the circular regions marked by white dotted lines. Green channel: CaM staining. Red channel: PI staining. (Scale bar: 100 μm) (B) Cell viability of PC-3 cells under different treatments with increasing concentration of PGL using CCK-8 assay. (*P < 0.05 versus PGL-MBs only, #P < 0.05 versus PGL-MBs+LFUS+Laser)

Animal experiments

CEUS in vivo

Encouraged by the excellent PDT efficacy *in vitro*, *in vivo* animal experiments using PC-3 a subcutaneous tumor model was further carried out. Before PDT treatment, CEUS was first performed *in vivo* to validate the contrast enhancement of PGL-MBs. After intravenous administration of PGL-MBs, abundant tumor microvessels were displayed clearly with an obviously enhanced signal-to-noise ratio (Figure 5A), achieving an enhanced diagnostic localization effect compared to traditional two-dimensional US imaging. Next, LFUS (with the same parameters as those in the *in vitro* study) were applied locally to the tumor site under CEUS, and the destruction of MBs could be clearly observed (Supplementary Video S1). LFUS irradiation was persistently employed until the MBs were completely destructed (usually for 3-5 min). In addition, CEUS of the abdominal aorta was also carried out to analyze the circulation half-life of PGL-MBs, and the calculated result was 183±36 s according to the time-intensity curve.

Fluorescence imaging *in vivo*

Since the distribution of PGL cannot be displayed by CEUS after the destruction of the PGL-MBs, fluorescence imaging was then performed to trace the biodistribution of PGL after LFUS exposure. As shown in Figure 5B, the fluorescence intensity of the local tumor site was significantly enhanced until 24 h, and the accumulation of PGL at the tumor site was quite obvious after LFUS exposure compared with the control group without LFUS exposure. The fluorescence intensity of the PGL-NPs was maintained without an obvious decrease within 6 h after LFUS, which provided enough time for the subsequent PDT treatment. We speculated that this phenomenon was induced by the transformation of PGL-MBs into PGL-NPs, with the assistance of US to enhance the permeability of tumor tissue and uptake by cancer cells, resulting in long-term retention of PSs at the tumor site.

Furthermore, at 24 h after LFUS, the major organs were excised for *ex vivo* fluorescence imaging to confirm the accumulation of PGL, and the results showed that the fluorescence intensity of the tumor tissue was much higher than that of the control group (Figure 5C). Quantitative analysis of the fluorescence signal (Figure 5D) revealed that the tumor signal was much higher than the liver signal. In contrast, for the mice without LFUS exposure, PGL was mainly retained in the liver. Thus, PGL-MBs were confirmed to efficiently accumulate at the tumor site with US exposure.

PDT in vivo

Motivated by the US-mediated high accumulation of PGL-MBs in the tumor tissue, *in vivo* PDT was carried out using the PC-3 subcutaneous tumor model. Treatment began when the tumor volume reached 100-120 mm^3 (usually 10-14 days after the subcutaneous inoculation of PC-3 cells). The PC-3 tumor-bearing mice were randomly divided into 8 groups. Then, PBS or PGL-MBs solutions were

intravenously injected (dose of PGL was 5 mg/kg) and combined with four different treatments (neither LFUS nor laser, LFUS only, laser only, or LFUS followed by laser). LFUS irradiation was then performed under monitoring by CEUS, and the mice receiving laser treatment were irradiated by a 650±5 nm laser at a power density of 0.2 W/cm^2 for 30 min at 4 h after LFUS exposure, at which time the tumor accumulation of PGL-MBs was still high. To investigate the pathological changes within the tumors, a mouse from each group was sacrificed at 24 h after treatment, and the tumors were excised, paraffin embedded and sectioned for H&E and TUNEL staining. The results of the H&E-stained tumor slices revealed obvious cell apoptosis and necrosis only in the LFUS-assisted PDT group (PGL-MBs injection combined with LFUS and laser) (Figure 6A). In addition, the results of TUNEL staining (Figure 6B) demonstrated the presence of apoptotic cells (stained as green fluorescence) in the same group. In contrast, there was scarce apoptosis in the other groups, demonstrating the effectiveness of the LFUS-assisted PDT treatment.

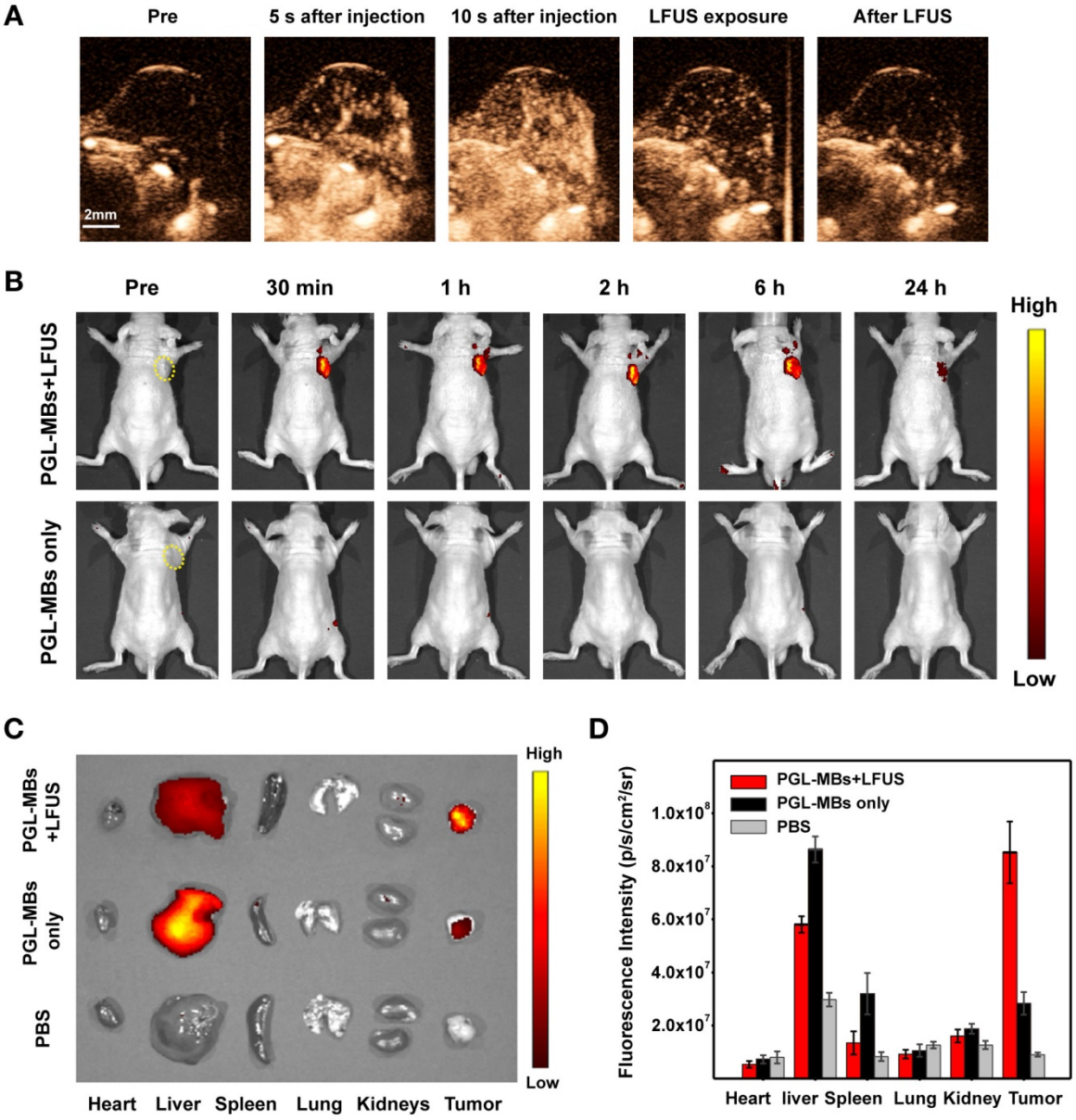

Figure 5. *In vivo* CEUS and fluorescence imaging in a subcutaneous PC-3 tumor model. (A) *In vivo* CEUS in a subcutaneous PC-3 tumor model. CEUS imaging of the tumor site before (pre) and after intravenous administration (i.v.) of PGL-MBs. (B) Fluorescence imaging *in vivo* at different time points after intravenous administration of PGL-MBs, with or without LFUS (400 kPa, 3 min) exposure. Tumors are circled with yellow dashed lines. (C) Images of organs excised at 24 h after injection. Organs of tumor-bearing mice without PGL-MBs injection were excised as negative controls. (D) Quantitative analysis of fluorescence intensity for the excised organs (n = 3).

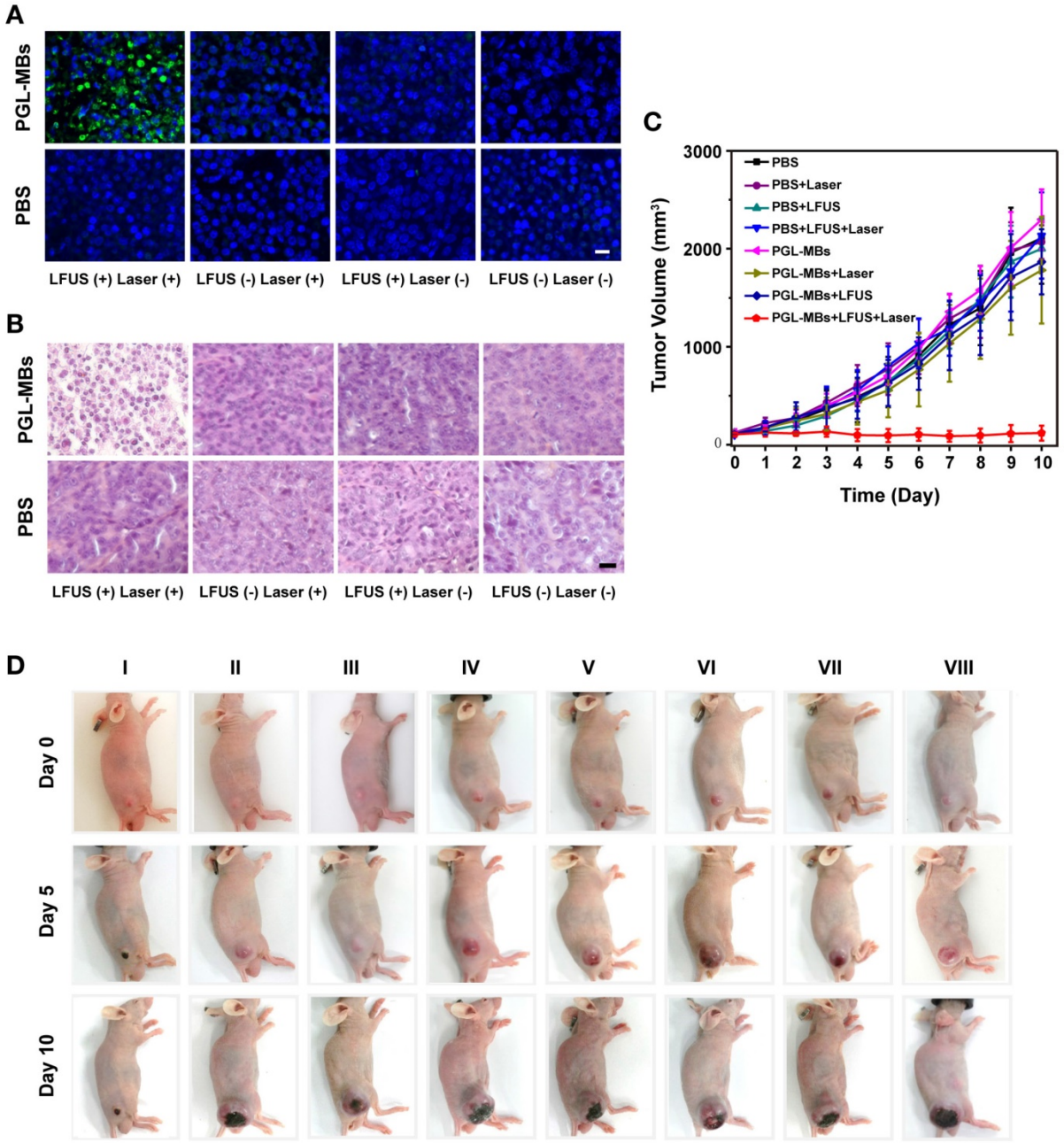

Figure 6. Therapeutic effects of PDT *in vivo* in the PC-3 xenograft-bearing mice. (A) *TUNEL* and (B) H&E staining of tumor slices excised at 24 h after the treatment. (Scale bar: 50 μm) (C) Tumor growth-curves calculated by caliper measurements every day after treatments. (n = 6) (D) Representative photographs showing therapeutic response of the mice after various treatments. (Groups: I. PGL-MBs+LFUS+Laser; II. PGL-MBs+LFUS; III. PGL-MBs+Laser; IV. PGL-MBs only; V. PBS+LFUS+Laser; VI. PBS+LFUS; VII. PBS+Laser; VIII. PBS only.)

Tumor sizes and body weights of the mice were measured every day to evaluate the long-term therapeutic effect. When the tumor volume reached 2000 mm^3, the mice were sacrificed out of ethical consideration. The results are shown in Figure 6C and 6D. Remarkably, the tumor volumes of mice treated with PGL-MBs+LFUS+laser showed a statistically significant difference from the other groups beginning at day 2 after treatment ($P < 0.05$), and the tumor growth in this group was completely inhibited within 10 days of observation. In contrast, tumors on mice that received the other treatments showed little growth inhibition, similar to the PBS group ($P > 0.05$). Notably in our experiment, mice showed no body weight loss after receiving the different treatments (Figure S4). In addition, H&E-stained images of the major organs from each group collected at day 10 after injection indicated no appreciable abnormalities or noticeable organ damage (Figure S5), indicating the biocompatibility of PGL-MBs. Thus, our results demonstrated that novel PGL-MBs used for CEUS/ fluorescence-guided and LFUS-assisted PDT could

offer an obvious therapeutic benefit, and moreover, this strategy was biocompatible and imposed no significant toxic side effects on the treated mice.

Discussion

In this study, we developed a novel PGL-MB platform for achieving US-controlled PS accumulation and enhanced PDT efficacy in PCa treatment. This PGL-MB-based and US-assisted PDT strategy (here, US means not only CEUS but also LFUS) exhibited excellent therapeutic efficacy both *in vitro* and *in vivo*. The results of *in vivo* PDT showed that only the LFUS-assisted PDT group exhibited obvious tumor growth inhibition, validating the feasibility and validity of our strategy. It should be noted that there was a negligible effect on tumor growth inhibition for the PGL-MBs combined with the laser only (without LFUS) *in vivo*. This phenomenon differed from the results of cell assays, which showed an obvious reduction in cell viability in the same group. The difference is easily comprehensible since PGL-MBs were incubated with tumor cells for an extended period of time (4 h) when conducting the cell assays, while in the animal experiments, PGL-MBs were limited within the vessels after intravenous administration and could rarely make contact with tumor cells. In addition, the *in vivo* laser irradiation was performed several hours after the injection when there were scarcely any PGL-MBs in the vessels. As a result of insufficient PS accumulation, both the tumor cells and vessels showed no obvious response to photodynamic damage. These results demonstrated the significance of UTMD (achieved by LFUS), which was a key determinant in the PGL-MBs-based PDT process, with the ability to control the accumulation of PSs and determine the success of PDT *in vivo*. It also should be noted that for the PGL-MBs+LFUS (without laser) group, there was no significant $^1O_2$ generation or cytotoxicity in the cell assays and no significant tumor growth inhibition in the animal experiments, indicating that LFUS didn't cause significant sonodynamic effect and sono-dynamic therapy didn't contribute to the therapeutic effect. Additionally, the temperature of the PGL-NPs solution and the tumor did not increase significantly during the PDT process (Figure S6), demonstrating there was also no photothermal effect involved in the PDT process.

UTMD has been used for targeted delivery of various chemotherapeutics (in chemotherapy) [29, 30], nucleic acids (in gene therapy) [31-33], photothermal therapeutic agents [34, 35] etc. Numerous studies have suggested that insonated MBs could enhance vascular permeability and cell membrane permeability [19, 36]. Our previous study validated that UTMD could enhance drug and gene delivery into the deep sites of tumor tissue by increasing the permeability of both the capillary endothelium and intratumoral extracellular matrix [37]. By virtue of these advantages of UTMD, controlled PS accumulation was achieved successfully in this study. Such accumulation of PSs at tumor sites is crucial for PDT, and this process determines the selectivity, efficacy and safety of the treatment. Compared to conventional, passive accumulation of PS-loaded nanoparticles, which is totally dependent on the enhanced permeability and retention (EPR) effect and is unpredictably influenced by many factors (such as tumor type, tumor microenvironment and properties of nanoparticles) [38], US-controlled accumulation shown here was highly efficient and more controllable. In this study, the accumulation of PGL was validated by fluorescence imaging. However, it should be noted that the type of tissue has great influence on light penetration and the fluorescence quantification shown here may be underestimated. In organs such as the liver, the fluorescence intensity might be influenced by the presence of hemoglobin, especially for *in vivo* imaging (Figure 5B), and thus the results of *ex vivo* imaging (Figure 5C and 5D) might be more precise.

Apart from the UTMD technique, the PGL-MBs were also the primary means of PS accumulation. To the best of our knowledge, PGL-MBs are the first reported porphyrin-loaded MBs used for PDT. As previously mentioned, the ingenious structure of PGL endows PGL-MBs with the superiorities of high PS loading content and resistance to PSs self-quenching caused by π-π interactions. These features could overcome the shortcomings of conventional PS-loaded MBs. In addition, owing to the amphipathicity of PGL, PGL-MBs after US destruction transformed into small nanoparticles, which then passed through the gaps between epithelial cells of tumor vessels and entered the tumor cells. All of these factors ensured sufficient accumulation of PGL and subsequent exertion of phototoxic effects at the tumor site.

Image guidance plays an imperative role when conducting PDT treatment, especially for deep tumors such as prostate cancer [13]. Among the imaging modalities used for PCa management, magnetic resonance imaging (MRI) has better diagnostic perfo-rmance than other modalities; however, the time-consuming process and high cost limit its application in guiding PDT, and some patients may have contraindications to undergoing MRI. Transrectal imaging (TRUS) is most widely used due to its real-time capability, portability, universality, low cost, and excellent safety (i.e., no ionizing radiation). TRUS-guided biopsy is the "gold

standard" for the diagnosis of PCa [39], and TRUS is also commonly used for guiding PDT of PCa [40]. However, the diagnostic efficiency of traditional B-mode US imaging is quite limited because of its difficulty in visualizing the cancerous lesions. Here, we used PGL-MBs to perform CEUS imaging, which provided blood perfusion information about the tumor and improved the diagnostic efficiency of traditional US [41-43]. In addition, since PGL was a component of the MBs, CEUS could actually trace the real-time distribution of the PS (PGL) in blood circulation. As a result, the UTMD process could be conducted at the right place (tumor sites) and at the right time with the help of CEUS monitoring.

This study presents exciting preliminary results and represents a significant step toward establishing a versatile therapeutic platform (PGL-MB) for PDT of PCa. Here, PGL-MBs served two functions: their application with CEUS enhanced the sensitivity of cancerous lesion detection, and US-controlled accumulation of PGL ensured the selectivity of PDT. Compared to conventional PDT of PCa, this strategy has made great progress in controlling PS accumulation and improving the diagnostic rate of PCa, both of which could enhance PDT efficacy. This strategy does indeed hold great promise in clinical PCa management for its ability to reduce treatment-related side effects by minimizing damage caused to the prostate and adjacent structures and to retain the benefits of treating cancer. Especially for the patients who want to be treated and not placed on an active surveillance regimen, this strategy might be a favorable alternative treatment. Furthermore, PGL-MBs exhibited a favorable biocompatibility both in cell assays and animal experiments, ensuring the safety of this treatment and indicating the feasibility of PGL-MBs in clinical translation.

However, our results were mainly based on PC-3 subcutaneous xenografts and additional studies are needed to reach our ultimate goal of applying this US-controlled PDT strategy in patients with prostate cancer. Next, orthotopic tumor models will be established to get closer to future clinical translation. In addition, given that the diagnostic specificity of CEUS for PCa is limited, using ultrasonic molecular imaging by conjugating ligands on PGL-MBs to make them more specifically bind prostate cancer tissue or using MRI/CEUS fusion imaging might be good directions for our future research, so the diagnostic efficiency of PCa can be improved as much as possible. In this study, fluorescence imaging was also used for validating the accumulation of PSs, however, *in vivo* fluorescence imaging of internal tumors such as prostate cancer (especially in the human body) is still difficult due to the limited depth of optical penetration and immature imaging instrumentation. Techniques such as endoscopy and laparoscopic systems might be helpful and used for *in vivo* fluorescence imaging.

In conclusion, as a novel theranostic platform with a favorable CEUS effect, PGL-MBs can be transformed into PGL-NPs under LFUS exposure and possess exceptional accumulation ability at the tumor site to achieve excellent therapeutic efficacy of PDT in PCa. With the elegant marriage between PGL-MBs and US, we have established a novel MB-based and US-assisted PDT strategy. This strategy will bring new hope to the future fight against cancer using theranostic MBs.

Abbreviations

PGL: porphyrin-grafted lipid; MBs: microbubbles; PGL-MBs: porphyrin-grafted lipid microbubbles; PGL-NPs: porphyrin-grafted lipid nanoparticles; PCa: prostate cancer; PSs: photosensitizers; PDT: photodynamic therapy; LFUS: low-frequency ultrasound; CEUS: contrast-enhanced ultrasound; US: ultrasound; UTMD: ultrasound-targeted microbubble destruction; CCK-8: cell counter kit-8; ADPA: 9,10-anthracenedipropionic acid; HUVECs: human umbilical vein endothelial cells; calcein-AM: calcein acetoxymethyl ester; PI: propidium iodide; H&E: hematoxylin and eosin; TUNEL: Terminal-deoxynucleoitidyl Transferase Mediated Nick End Labeling.

Acknowledgements

This work was supported by the National Key Research and Development Program of China (No. 2016YFA0201400), Science and Technology Program of Guangzhou (No. 201704020164), National Key R&D Program of China (No. 2017YFC0112000), National Natural Science Foundation of China (Grant No, 81430038, 81571810, 81201186, 81771846), State Key Program of National Natural Science of China (No. 81230036), grants from Peking University Third Hospital (BYSY2015023), the China Postdoctoral Science Foundation (2013M530014) and the Foundation for Innovative Research Groups of the National Natural Science Foundation of China (No. 81421004).

Author contributions

Z.D., X.L. and Y.Y. designed the study; X.L. performed the chemical synthesis experiments. Y.Y. and Q.C. performed the animal experiments; C.G. and X.W. performed the cell experiments; Y.Y. and X.L. wrote the paper. T.Y., M.Y., E.Q., R.Z. and Z.D edited the manuscript; Z.D. and R.Z. supervised the whole project.

Supplementary Material

Supplementary figures.
http://www.thno.org/v08p1665s1.pdf
Supplementary video S1.
http://www.thno.org/v08p1665s2.mp4

Competing Interests

The authors have declared that no competing interest exists.

References

1. Siegel RL, Miller KD, Jemal A. Cancer statistics, 2015. CA Cancer J Clin. 2015; 65: 5-29.
2. Chen W, Zheng R, Baade PD, Zhang S, Zeng H, Bray F, et al. Cancer statistics in China, 2015. CA Cancer J Clin. 2016; 66: 115-32.
3. Esserman LJ, Thompson IM, Reid B, Nelson P, Ransohoff DF, Welch HG, et al. Addressing overdiagnosis and overtreatment in cancer: a prescription for change. Lancet Oncol. 2014; 15: e234-42.
4. Klotz L, Emberton M. Management of low risk prostate cancer-active surveillance and focal therapy. Nat Rev Clin Oncol. 2014; 11: 324-34.
5. Wadman M. Treatment: When less is more. Nature. 2015; 528: S126-7.
6. Castano AP, Mroz P, Hamblin MR. Photodynamic therapy and anti-tumour immunity. Nat Rev Cancer. 2006; 6: 535-45.
7. Daniell MD, Hill JS. A history of photodynamic therapy. Aust N Z J Surg. 1991; 61: 340-8.
8. Dolmans DE, Fukumura D, Jain RK. Photodynamic therapy for cancer. Nat Rev Cancer. 2003; 3: 380-7.
9. Azzouzi AR, Barret E, Moore CM, Villers A, Allen C, Scherz A, et al. TOOKAD((R)) Soluble vascular-targeted photodynamic (VTP) therapy: determination of optimal treatment conditions and assessment of effects in patients with localised prostate cancer. BJU Int. 2013; 112: 766-74.
10. Patel H, Mick R, Finlay J, Zhu TC, Rickter E, Cengel KA, et al. Motexafin lutetium-photodynamic therapy of prostate cancer: short- and long-term effects on prostate-specific antigen. Clin Cancer Res. 2008; 14: 4869-76.
11. Moore CM, Azzouzi AR, Barret E, Villers A, Muir GH, Barber NJ, et al. Determination of optimal drug dose and light dose index to achieve minimally invasive focal ablation of localised prostate cancer using WST11-vascular-targeted photodynamic (VTP) therapy. BJU Int. 2015; 116: 888-96.
12. Azzouzi AR, Vincendeau S, Barret E, Cicco A, Kleinclauss F, van der Poel HG, et al. Padeliporfin vascular-targeted photodynamic therapy versus active surveillance in men with low-risk prostate cancer (CLIN1001 PCM301): an open-label, phase 3, randomised controlled trial. Lancet Oncol. 2017; 18: 181-91.
13. Moore CM, Pendse D, Emberton M. Photodynamic therapy for prostate cancer--a review of current status and future promise. Nat Clin Pract Urol. 2009; 6: 18-30.
14. Lindner U, Lawrentschuk N, Trachtenberg J. Image guidance for focal therapy of prostate cancer. World J Urol. 2010; 28: 727-34.
15. Bouchelouche K, Turkbey B, Choyke PL. Advances in imaging modalities in prostate cancer. Curr Opin Oncol. 2015; 27: 224-31.
16. Sporea I, Badea R, Popescu A, Sparchez Z, Sirli RL, Danila M, et al. Contrast-enhanced ultrasound (CEUS) for the evaluation of focal liver lesions - a prospective multicenter study of its usefulness in clinical practice. Ultraschall Med. 2014; 35: 259-66.
17. Sidhu PS, Choi BI, Nielsen MB. The EFSUMB Guidelines on the Non-hepatic Clinical Applications of Contrast Enhanced Ultrasound (CEUS): a new dawn for the escalating use of this ubiquitous technique. Ultraschall Med. 2012; 33: 5-7.
18. Uemura H, Sano F, Nomiya A, Yamamoto T, Nakamura M, Miyoshi Y, et al. Usefulness of perflubutane microbubble-enhanced ultrasound in imaging and detection of prostate cancer: phase II multicenter clinical trial. World J Urol. 2013; 31: 1123-8.
19. Hernot S, Klibanov AL. Microbubbles in ultrasound-triggered drug and gene delivery. Adv Drug Deliv Rev. 2008; 60: 1153-66.
20. Lentacker I, De Cock I, Deckers R, De Smedt SC, Moonen CT. Understanding ultrasound induced sonoporation: definitions and underlying mechanisms. Adv Drug Deliv Rev. 2014; 72: 49-64.
21. Lucky SS, Soo KC, Zhang Y. Nanoparticles in photodynamic therapy. Chem Rev. 2015; 115: 1990-2042.
22. Klibanov AL, Shevchenko TI, Raju BI, Seip R, Chin CT. Ultrasound-triggered release of materials entrapped in microbubble-liposome constructs: a tool for targeted drug delivery. J Control Release. 2010; 148: 13-7.
23. Liang X, Li X, Jing L, Yue X, Dai Z. Theranostic porphyrin dyad nanoparticles for magnetic resonance imaging guided photodynamic therapy. Biomaterials. 2014; 35: 6379-88.
24. Jing L, Liang X, Li X, Lin L, Yang Y, Yue X, et al. Mn-porphyrin conjugated Au nanoshells encapsulating doxorubicin for potential magnetic resonance imaging and light triggered synergistic therapy of cancer. Theranostics. 2014; 4: 858-71.
25. Liang X, Li X, Yue X, Dai Z. Conjugation of porphyrin to nanohybrid cerasomes for photodynamic diagnosis and therapy of cancer. Angew Chem Int Ed Engl. 2011; 50: 11622-7.
26. Yin T, Wang P, Zheng R, Zheng B, Cheng D, Zhang X, et al. Nanobubbles for enhanced ultrasound imaging of tumors. Int J Nanomedicine. 2012; 7: 895-904.
27. Hackbarth S, Horneffer V, Wiehe A, Hillenkamp F, Röder B. Photophysical properties of pheophorbide- a -substituted diaminobutane poly-propylene-imine dendrimer. Chem Phys. 2001; 269: 339-46.
28. Huynh E, Leung BY, Helfield BL, Shakiba M, Gandier JA, Jin CS, et al. In situ conversion of porphyrin microbubbles to nanoparticles for multimodality imaging. Nat Nanotechnol. 2015; 10: 325-32.
29. Unger E, Porter T, Lindner J, Grayburn P. Cardiovascular drug delivery with ultrasound and microbubbles. Adv Drug Deliv Rev. 2014; 72: 110-26.
30. Sirsi SR, Borden MA. State-of-the-art materials for ultrasound-triggered drug delivery. Adv Drug Deliv Rev. 2014; 72: 3-14.
31. Rychak JJ, Klibanov AL. Nucleic acid delivery with microbubbles and ultrasound. Adv Drug Deliv Rev. 2014; 72: 82-93.
32. Chertok B, Langer R, Anderson DG. Spatial Control of Gene Expression by Nanocarriers Using Heparin Masking and Ultrasound-Targeted Microbubble Destruction. ACS nano. 2016; 10: 7267-78.
33. Yin T, Wang P, Li J, Zheng R, Zheng B, Cheng D, et al. Ultrasound-sensitive siRNA-loaded nanobubbles formed by hetero-assembly of polymeric micelles and liposomes and their therapeutic effect in gliomas. Biomaterials. 2013; 34: 4532-43.
34. Guo C, Jin Y, Dai Z. Multifunctional ultrasound contrast agents for imaging guided photothermal therapy. Bioconjug Chem. 2014; 25: 840-54.
35. Zha Z, Wang S, Zhang S, Qu E, Ke H, Wang J, et al. Targeted delivery of CuS nanoparticles through ultrasound image-guided microbubble destruction for efficient photothermal therapy. Nanoscale. 2013; 5: 3216-9.
36. Kooiman K, Vos HJ, Versluis M, de Jong N. Acoustic behavior of microbubbles and implications for drug delivery. Adv Drug Deliv Rev. 2014; 72: 28-48.
37. Yin T, Wang P, Li J, Wang Y, Zheng B, Zheng R, et al. Tumor-penetrating codelivery of siRNA and paclitaxel with ultrasound-responsive nanobubbles hetero-assembled from polymeric micelles and liposomes. Biomaterials. 2014; 35: 5932-43.
38. Maeda H. Toward a full understanding of the EPR effect in primary and metastatic tumors as well as issues related to its heterogeneity. Adv Drug Deliv Rev. 2015; 91: 3-6.
39. Heidenreich A, Bastian PJ, Bellmunt J, Bolla M, Joniau S, van der Kwast T, et al. EAU guidelines on prostate cancer. part 1: screening, diagnosis, and local treatment with curative intent-update 2013. Eur Urol. 2014; 65: 124-37.
40. Azzouzi AR, Lebdai S, Benzaghou F, Stief C. Vascular-targeted photodynamic therapy with TOOKAD(R) Soluble in localized prostate cancer: standardization of the procedure. World J Urol. 2015; 33: 937-44.
41. Kundavaram CR, Halpern EJ, Trabulsi EJ. Value of contrast-enhanced ultrasonography in prostate cancer. Curr Opin Urol. 2012; 22: 303-9.
42. Sano F, Uemura H. The utility and limitations of contrast-enhanced ultrasound for the diagnosis and treatment of prostate cancer. Sensors (Basel). 2015; 15: 4947-57.
43. Cantisani V, Bertolotto M, Weskott HP, Romanini L, Grazhdani H, Passamonti M, et al. Growing indications for CEUS: The kidney, testis, lymph nodes, thyroid, prostate, and small bowel. Eur J Radiol. 2015; 84: 1675-84.